Scientific Reports

https://doi.org/10.1038/s41598-026-43316-y

Article in Press

Interfacial engineering of aluminum powder with a tannic acid/Fe^3 complex and fluorosilane for high-performance energetic composites

Received: 9 December 2025

Accepted: 3 March 2026

Published online: 07 March 2026

Cite this article as: Liu B., Gou X., Li Y. *et al.* Interfacial engineering of aluminum powder with a tannic acid/Fe^3 complex and fluorosilane for high-performance energetic composites. *Sci Rep* (2026). https://doi.org/10.1038/s41598-026-43316-y

Bo Liu, Xiaodong Gou, Yingjun Li, Jiahao Liang, Shi Yan, Xueyong Guo & Jianxin Nie

Interfacial Engineering of Aluminum Powder with a Tannic Acid/Fe^{3+} Complex and Fluorosilane for High-Performance Energetic Composites

Bo Liu,[a] Xiaodong Gou,[a] Yingjun Li,[b] Jiahao Liang,[a] Shi Yan,[a] Xueyong Guo,[a] Jianxin Nie,*[a]

a State Key Laboratory of Explosion Science and Technology, Beijing Institute of Technology, Beijing, 100081, China.

b 601 Institute, The Six Academy of China Aerospace Science and Industry Corporation, Hohhot, 010076,China.

* Corresponding authors. E-mail address: niejx@bit.edu.cn (J. X. Nie).

Abstract

Constructing a multifunctional coating on aluminum (Al) powder is crucial for enhancing its energy release in propellants. However, existing methods face challenges such as complex processes, high costs, and poor controllability. This study proposes a simple self-assembly strategy to construct a dual core-shell structure on aluminum powder surfaces, consisting of an inner tannic acid-Fe^{3+} (TA-Fe) network and an outer fluorosilane (PDTTS) layer, thus successfully fabricating the Al@TA-Fe@PDTTS composite. Molecular dynamics simulations reveal a strong binding energy among the coating components, providing theoretical support for the successful realization of the self-assembly process. The resulting Al@TA-Fe@PDTTS composite exhibits excellent hydrophobicity (contact angle up to 123.7°) and significantly promotes the cracking of the inert alumina shell. Serving as a combined fuel and catalyst, the composite significantly lowers the high-temperature decomposition peak of ammonium perchlorate (AP) by 41.9 °C. Furthermore, laser ignition tests confirm a substantially shortened ignition delay (from 13.2

ms for aluminum/AP mixtures to only 4.8 ms for the composite material) and a more intense combustion process, highlighting its great potential for advanced energetic applications.

Key words: aluminum powder; dual core-shell structure; interface performance; combustion; ammonium perchlorate.

1. Introduction

Aluminum powder is widely used in the formulation of solid propellants due to its high energy density (30.98 kJ·mol^{-1}), active chemical properties, low price, and good compatibility with other materials in the propellant[1-4].The incorporation of aluminum powder into composite solid propellants enhances combustion stability and substantially increases propellant density and specific impulse, thereby yielding greater overall thrust output for rockets within an equivalent volume[5-8]. However, aluminum will spontaneously react with oxygen in the air to form a layer of aluminum oxide film with a thickness of several nanometers, which wraps the surface of the aluminum particles[9]. Since aluminum oxide has a high melting point (2054 ℃) and boiling point (2980 ℃), and low thermal conductivity, it will hinder the mass diffusion and interfacial reaction between the oxidant and aluminum powder, and hinder heat and mass transfer, thereby increasing the ignition temperature and ignition delay time of aluminum powder[10-12].

Over the past several decades, the predominant approach to enhancing the combustion performance of aluminum powder has been the introduction of fluorine-containing compounds. Fluorine not only reacts easily with aluminum, but also has been shown to stimulate the surface pre-ignition exothermic reaction with the Al_2O_3 shell[13-15], promoting the production of low-boiling point AlF_3 substances. Therefore, fluorine-containing compounds such as polytetrafluoroethylene (PTFE)[16-17], polyvinylidene fluoride (PVDF)[18-21], perfluoric acid[22-23], and ammonium perfluorooctanoate (APFO)[24] etc. are

used to improve the combustion performance of aluminum powder. While ball milling has been used to combine fluorine-containing compounds with aluminum powder[25-26], this approach often alters the original spherical morphology of the aluminum particles, which can negatively affect their packing density, rheology, and ultimately their performance in propellant formulations. It should be noted, however, that recent advances in specialized milling techniques, such as emulsion-assisted milling, have demonstrated the possibility of obtaining spherical aluminum composites with tunable morphology and enhanced reactivity while mitigating some of the traditional drawbacks of milling[27]. Despite this progress, achieving intimate contact between the fluorine source and the aluminum surface without compromising particle morphology or introducing complex processing steps remains a challenge. Therefore, considerable research interest persists in modifying the aluminum powder surface by directly coating fluorine-containing compounds onto the particles. This approach aims to ensure full contact between the fluorine species and aluminum while preserving the original particle morphology, thereby effectively enhancing combustion performance. At present, some studies have coated some materials (PTFE, PVDF, polydopamine (PDA), etc.) on the surface of aluminum powder particles to improve the combustion performance of aluminum powder. However, the method of coating the surface of aluminum powder also has many problems: the preparation method is complicated, the raw materials or preparation method are expensive, and the preparation process is difficult to control.

Another important component in composite propellants is the oxidizer ammonium perchlorate (AP). The combustion performance of composite propellants is closely related to the thermal decomposition process of AP. The ignition delay time of the propellant can be shortened and the combustion rate can be increased by reducing the peak temperature of AP decomposition[28-31]. A large number of studies have shown that transition metal ion salts or transition metal ion compounds can effectively reduce the thermal

decomposition temperature of AP[32-35]. However, these often require complex methods or specialized equipment to prepare.

Therefore, in this work, we propose a novel interfacial engineering strategy that concurrently addresses the dual challenges of the inert Al_2O_3 shell and the poor interfacial compatibility. We successfully constructed a dual core-shell structured Al@TA-Fe@PDTTS composite. The design philosophy is twofold: the inner TA-Fe network, formed via the facile self-assembly of low-cost tannic acid and Fe^{3+} ions, is engineered to interact strongly with the native alumina layer and serve as a catalytic site. The outer fluorosilane (PDTTS) layer is designed to confer superior hydrophobicity and, upon decomposition, provide reactive fluorine species that corrode the oxide shell and promote its cracking. This rational design, verified by molecular dynamics simulations, not only ensures a robust coating architecture but also synergistically enhances both the reactivity and interfacial properties of aluminum. This work provides a new insight into the molecular-level interface control for designing advanced multifunctional metal fuels, offering a simple and effective pathway towards high-performance energetic composites.

2. Experimental section

2.1 Materials

Aluminum powder was supplied by Hengda Aluminum Co., Ltd. (median particle size D_{50} = 5 μm; average particle size ≈ 4 μm, as shown Fig.S1). Ammonium perchlorate was purchased from Liming Research Institute of Chemical Industry. Tannic acid (98%) □ 1H,1H,2H,2H-Perfluorodecyltriethoxysilane (PDTTS) (98%), $FeCl_3·6H_2O$ (99%),and n-Hexane (≥ 98%), Tris-Bis (99.5% purity), were purchased from Shanghai Macklin Biochemical Co., Ltd. Absolute ethanol (≥ 99.7%) was obtained from Shanghai Energy Chemical Co., Ltd. All chemicals are analytical grade.

2.2 Synthesis of Al@TA-Fe Composite

The Al@TA-Fe composite was fabricated via a facile one-pot coordination-driven self-assembly process. In a typical procedure, 0.4 g of TA was first dissolved in 200 mL of deionized water under magnetic stirring to form a clear solution. Subsequently, 2 g of raw Al powder was introduced into the TA solution and uniformly dispersed via ultrasonication for 10 min. Then, 20 mL of an aqueous $FeCl_3 \cdot 6H_2O$ solution (0.065 g) was added dropwise into the mixture, which was allowed to react for 20 min. This step facilitates the rapid formation of a coordinated TA-Fe network on the Al surface The pH of the mixture was then adjusted to 8.0 using a Tris-Bis buffer to optimize the coordination environment and strengthen adhesion. The resulting product was collected by filtration, thoroughly washed with deionized water, and dried overnight at ambient temperature to yield the Al@TA-Fe powder.

2.3 Construction of the Dual Core-Shell Structure (Al@TA-Fe@PDTTS)

To impart hydrophobicity and introduce reactive fluorine species, the as-prepared Al@TA-Fe composite was further functionalized with PDTTS. Briefly, 10 g of Al@TA-Fe was fully dispersed in 100 mL of n-hexane via ultrasonication. Then, 1 g of PDTTS was added dropwise into the suspension. The mixture was left to stand for 24 h, allowing the silane groups of PDTTS to condense with the residual hydroxyl groups on the TA-Fe surface, forming a robust covalent interface. The final product, denoted as Al@TA-Fe@PDTTS, was obtained by filtration, washed three times with n-hexane to remove unreacted precursors, and dried at 50°C. A schematic illustration of the overall fabrication process is presented in Fig. 1.The macroscopic morphologies of pure Al powder and A are shown in Fig.S2.

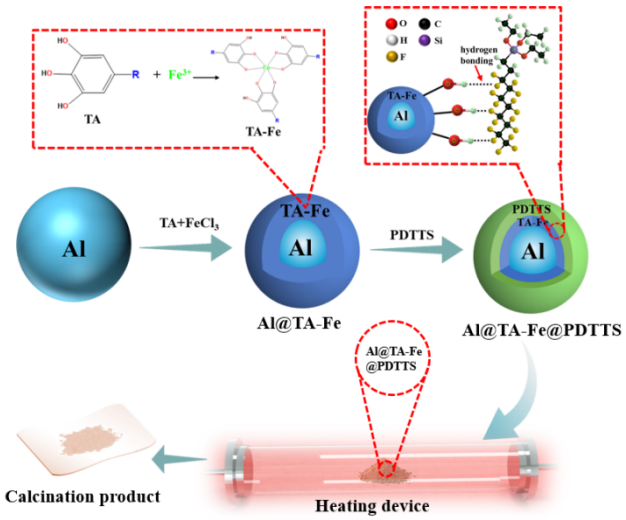

Fig.1 Schematic diagram of the preparation process and experimental process of Al@TA-Fe@PDTTS.

2.4 Characterization and Methods

The sample was observed using a ZEISS Sigma 300 scanning electron microscope (SEM) and a Tecnai G2 F30 S-TWIN transmission electron microscope (TEM). Powder X-ray diffraction (PXRD) was performed on a Panaco Emoyrean instrument using a Cu target, scanning from 5° to 90° at 10°·min^{-1}. Fourier transform infrared spectrometer (FT-IR) was performed using a Thermo Scientific Nicolet iS20 instrument. The test range is 4000 cm^{-1} to 400 cm^{-1}. X-ray Photoelectron Spectroscopy (XPS) was performed using a Thermo Scientific K-Alpha. The spot size is 400 μm, the working voltage is 12 kV, the filament current is 6 mA; the full spectrum scanning energy is 150 eV, and the step size is 1 eV. Thermal analyses, including differential scanning calorimetry (DSC) and thermogravimetric analysis (TGA), were conducted using a Mettler Toledo TGA/DSC 3+ instrument. The measurements were performed under a flowing argon atmosphere at constant heating rates of either 10 or 20 K·min^{-1}. The static contact angle was measured by the hypsometry method using the standard static drop method, using the JY-82B Kruss DSA type contact angle meter.

To investigate the combustion products of the sample in an air atmosphere,

200 mg of the sample was placed in a transparent tube furnace (air atmosphere), heated to 600 ℃ (or 800 ℃) at a rate of 20 ℃·min^{-1}, and kept warm for 10 min. The reaction products were collected after cooling to room temperature and characterize them by SEM and XRD.

TRHW-7000C automatic oxygen bomb calorimeter was used to test the combustion calorific value of the sample. The combustion calorific value of each sample is measured in parallel three times, and the average value is taken as the final result. In high-speed photography experiments, Al and Al@TA-Fe@PDTTS was physically uniformly mixed with AP in a mass ratio of 9:1. Then, ignition was achieved using a CO_2 laser system (30 W output, 500 ms duration), with a 100 mg sample loaded on the platform in air at atmospheric pressure. Combustion process were recorded using a high-speed camera configured for 10000 fps acquisition and a 50 ms exposure time per frame

2.5 Molecular Dynamics Simulation Methodology

Molecular dynamics (MD) simulations were performed to evaluate the binding ability among the core components (Al, TA, and PDTTS) and to provide theoretical support for the experimental design. The initial molecular models of Al, TA, and PDTTS were constructed using the Visualizer module within the Materials Studio software package, as shown in Fig.2(d), Fig.2(e) and Fig.2(f), respectively. To build the simulation systems, the Al model was expanded into a 4×4×2 supercell. Subsequently, three-dimensional periodic boxes containing 12 TA molecules and 30 PDTTS molecular chains, respectively, were generated using the Amorphous Cell module, as shown in Fig.2(d), Fig.2(e) and Fig.2(f), respectively. The composite interfacial models (Al/TA, Al/PDTTS, and Al/TA/PDTTS) were then geometrically optimized and subjected to MD simulations using the Forcite module.

All simulations employed the COMPASS II force field and were conducted under the NVT (canonical) ensemble. The temperature was maintained at 298 K. A time step of 0.1 fs was used for integration, with a total simulation time

of 1000 ps for each system. Data from the final 500 ps of the equilibrated trajectories were collected for subsequent binding energy analysis.

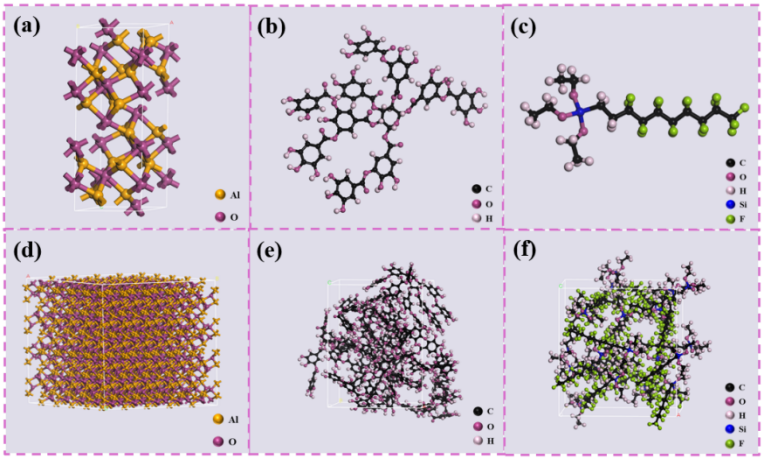

Fig. 2 (a) Molecular structure of Al; (b) Molecular structure of TA; (c) Molecular structure of PDTTS; (d) Supercell model of Al; (e) 3D amorphous cell (AC) box of TA; (f) 3D AC box of PDTTS.

3 Result and discussion

3.1. Binding energy

In this study, the binding energy (E_{bind}), a key metric for quantifying the strength of intermolecular interactions [36], can be derived from the intermolecular interaction energy (E_{inter}) as shown in equation (1):

$$E_{bind}=-E_{inter}=-(E_{A-B}-E_{A(A-B)}-E_{B(A-B)}) \quad (1)$$

In equation (1), E_{A-B} represents the total energy of the composite system; $E_{A(A-B)}$ represents the energy of A in the composite system, and $E_{B(A-B)}$ represents the energy of B in the composite system.

For a system to reach dynamic equilibrium, it is usually necessary to make the temperature and energy in the system reach equilibrium. In general, as long as the temperature and energy remain within the fluctuation range of 5% to 10%, it can be concluded that dynamic equilibrium has been achieved[37]. Fig.3 shows the fluctuation curves of temperature (Fig.3a-c) and energy (Fig.3d-f) during the molecular dynamics simulation of the systems Al_2O_3/TA, Al_2O_3/PDTTS, and Al_2O_3@TA/PDTTS. As time goes by, after 500ps, the

fluctuations of the temperature and energy of the system are within 5%, and the system reaches equilibrium. The above results show that all simulation systems have reached dynamic equilibrium, which ensures the reliability of subsequent data collection and analysis.

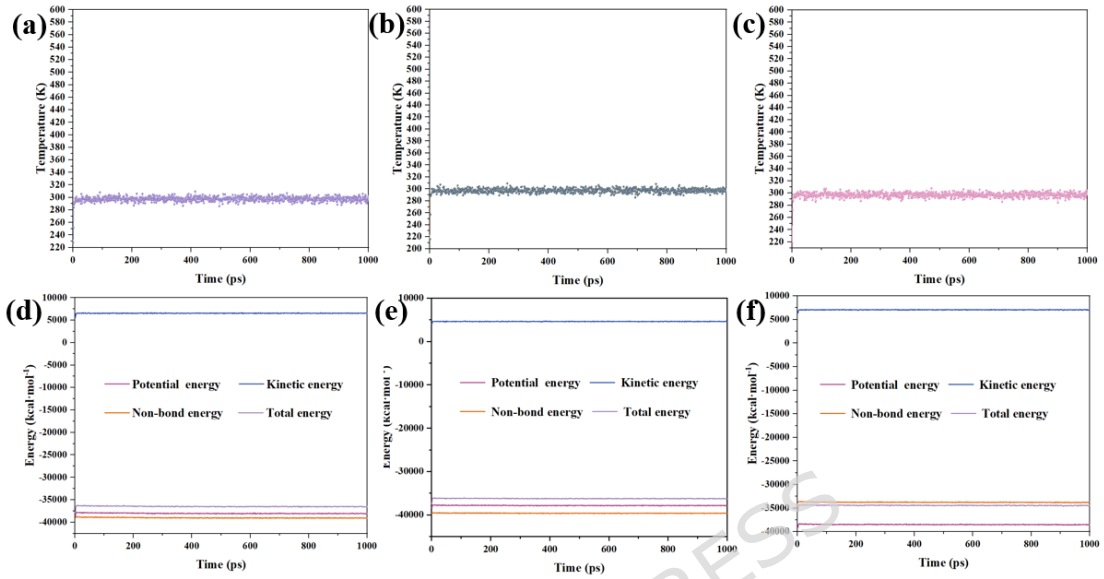

Fig. 3 (a) Temperature fluctuation curve of the Al_2O_3/TA system; (b) Temperature fluctuation curve of the Al_2O_3/PDTTS system; (c) Temperature fluctuation curve of the Al_2O_3@TA/PDTTS system; (d) Energy fluctuation curve of the Al_2O_3/TA system; (e) Energy fluctuation curve of the Al_2O_3/PDTTS system; (f) Energy fluctuation curve of the Al_2O_3@TA/PDTTS system.

Fig.4(a-d), Fig.4(b-e) and Fig.4(c-f) present the optimized molecular configurations and corresponding equilibrium structures for the hybrid systems Al_2O_3/TA, Al_2O_3/PDTTS and Al_2O_3@TA/PDTTS, respectively. The calculated binding energies for these systems are summarized in Table 1. Specifically, the Al_2O_3/TA, Al_2O_3/PDTTS, and Al_2O_3@TA/PDTTS systems exhibit binding energies of 782.36 kcal·mol^{-1}, 211.79 kcal·mol^{-1}, and 498.21 kcal·mol^{-1}, respectively.

These results indicate that TA molecules possess a strong affinity for the Al_2O_3 surface, which can be attributed primarily to the formation of hydrogen bonds between hydrogen atoms in TA and oxygen atoms in Al_2O_3. This interaction facilitates the effective coating of the TA interlayer onto the alumina shell. Moreover, the binding capability of PDTTS with TA is substantially greater than that with bare Al_2O_3. This enhanced adhesion arises

from the tendency of fluorine atoms in PDTTS to form hydrogen bonds with the hydroxyl groups present in TA, thereby strengthening the interfacial cohesion.

The simulation outcomes demonstrate that TA exhibits superior binding to the Al_2O_3 crystal surface compared to PDTTS. Conversely, PDTTS adheres more effectively to the TA-modified surface than to pristine Al_2O_3 particles. Collectively, these computational findings validate the rationality of the experimental design for constructing the dual-layer coating system.

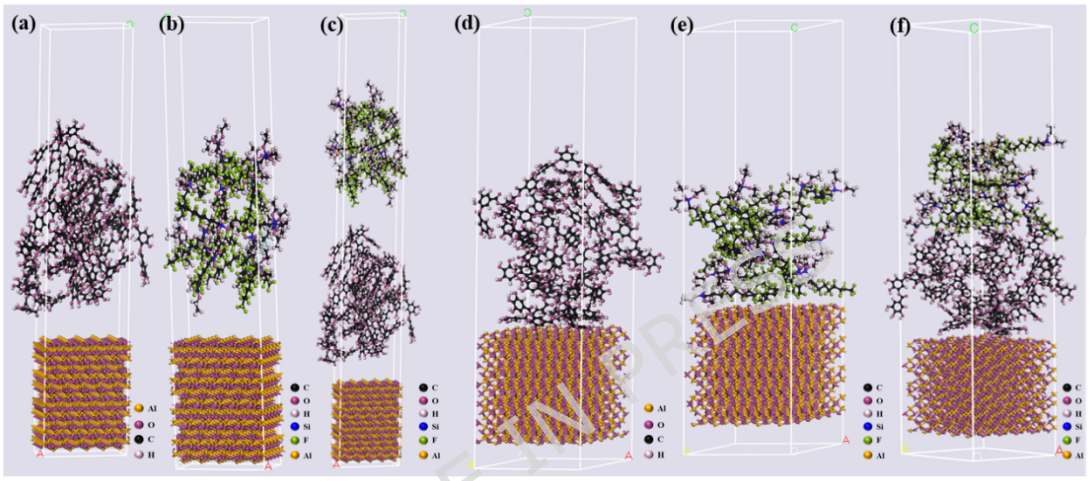

Fig.4 (a) Optimized model of the Al_2O_3/TA system; (b) Optimized model of the Al_2O_3/PDTTS system; (c) Optimized model of the Al_2O_3@TA/PDTTS system; (d) Final equilibrium structure of the Al_2O_3/TA system; (e) Final equilibrium structure of the Al_2O_3/PDTTS system; (f) Final equilibrium structure of the Al_2O_3@TA/PDTTS system.

Table 1 Binding energies of Al_2O_3/TA, Al_2O_3/PDTTS and Al_2O_3@TA/PDTTS

System	Al_2O_3/TA,	Al_2O_3/PDTTS	Al_2O_3@TA/PDTTS
Binding energy ($kcal \cdot mol^{-1}$)	782.36	211.79	498.21

3.2. Characterization of Al@TA-Fe@PDTTS

The microscopic morphologies of the different samples are presented in Fig.5. Pure Al particles (Fig.5a) and Al@PDTTS particles (Fig.5c) exhibit a relatively smooth and even topography. In contrast, the surfaces of Al@TA-Fe (Fig.5b) and the final composite Al@TA-Fe@PDTTS display a distinctly rougher texture compared to their counterparts. Higher-magnification imaging reveals the presence of numerous protrusions on the aluminum

particle surfaces, attributed to the variable thickness of the deposited TA-Fe coating layer. Furthermore, energy-dispersive X-ray spectroscopy (EDS) analysis of the Al@TA-Fe@PDTTS composite (Fig.5e) detects the presence of carbon (C), iron (Fe), silicon (Si), and fluorine (F) elements on the particle surfaces, which are absent in the raw Al powder. This elemental signature provides direct evidence for the successful establishment of both the inner TA-Fe and the outer PDTTS interfacial layers on the aluminum substrate.

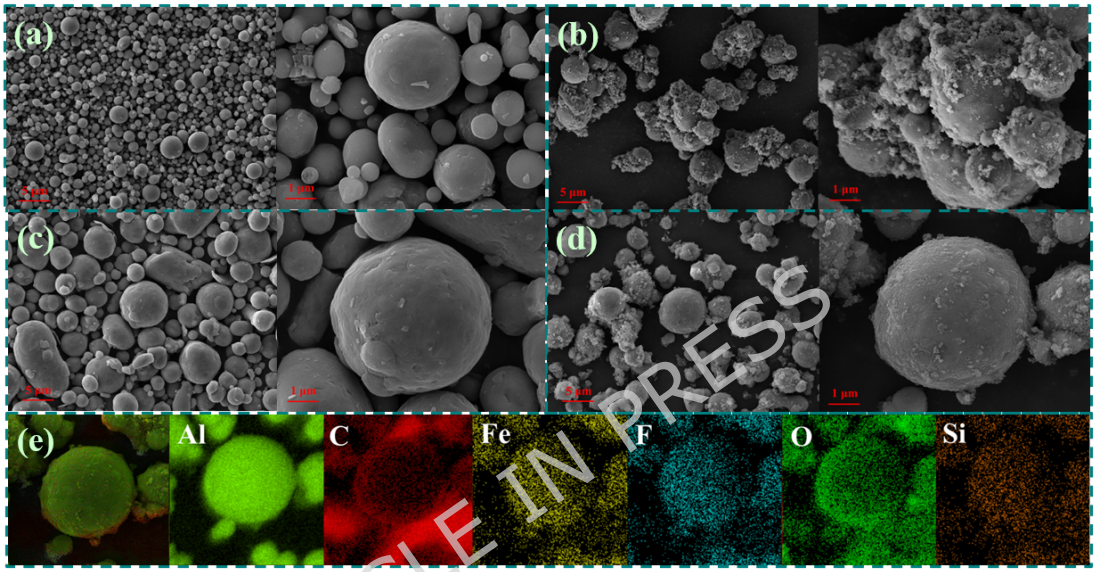

Fig.5 SEM images of (a) Al, (b) Al@TA-Fe (c) Al@PDTTS and (d) Al@TA-Fe@PDTTS; (e) EDS mapping of Al@TA-Fe@PDTTS.

To gain deeper insight into the morphological and compositional characteristics of the TA-Fe and PDTTS coatings on the aluminum powder, transmission electron microscopy (TEM) and energy-dispersive X-ray spectroscopy (EDS) mapping were performed on the Al@TA-Fe@PDTTS sample, with the results presented in Fig. 6. As can be seen from Fig.6(a) and Fig.6(b), there is an irregularly shaped coating layer on the surface of the aluminum powder particles. By correlating the high-resolution TEM image of a single particle's edge with the element energy spectrum surface scanning image (Fig.6(b-e)), the architecture of the composite particle can be clearly resolved. The microstructure is comprised of three distinct concentric regions: a central, black core corresponding to metallic aluminum (Al), surrounded by

a dark gray intermediate layer identified as the native aluminum oxide (Al_2O_3). Externally, both the TA-Fe and PDTTS functional layers are observed to reside on the outer surface of this oxide layer. According to Fig.6(b-e), the TA-Fe and PDTTS coating materials are deposited in a relatively even manner onto the aluminum powder particles. Collectively, the morphological and compositional data presented successfully verify the existence of the designed core-shell configuration in Al@TA-Fe@PDTTS.

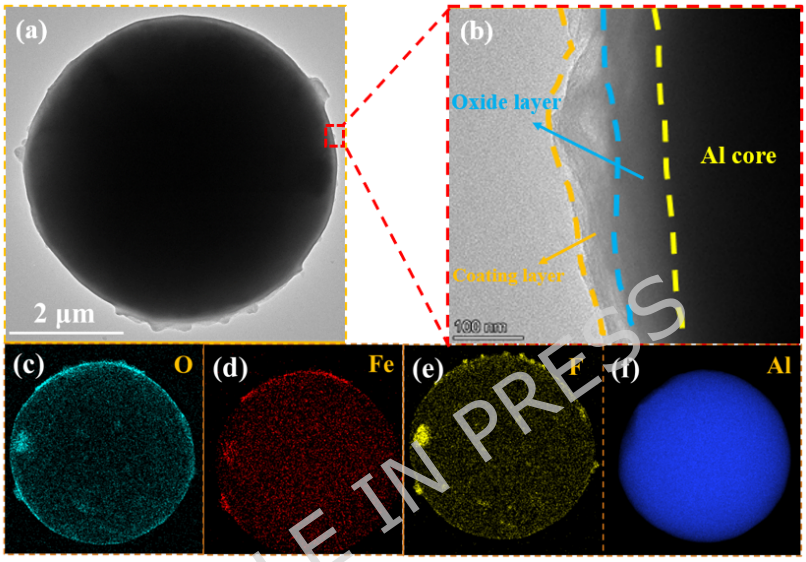

Fig.6 TEM image and energy spectrum scanning of Al@TA-Fe@PDTTS single particle.

The surface chemical composition of the Al@TA-Fe@PDTTS particles was further investigated using Fourier-transform infrared (FT-IR) spectroscopy (Fig.S3). The spectrum exhibits characteristic absorption bands corresponding to functional groups from both coating layers. Key signals include those attributed to PDTTS, such as the asymmetric stretching vibration of $-CF_2$ at 822 cm^{-1} and the Si-O-C absorption at 1055 cm^{-1} [38]. Concurrently, multiple bands originating from tannic acid (TA) are identified: the ester C-O stretch (1193 cm^{-1}) [39], aromatic ring C-C stretches (1572 and 1431 cm^{-1}), the carbonyl (C=O) stretch (1689 cm^{-1}), and a broad O-H stretching vibration (3351 cm^{-1}). An additional signal at 2937 cm^{-1} is assigned to the C-H asymmetric stretch in PDTTS. The co-presence of these distinctive vibrational fingerprints for both TA and PDTTS on the particle surface provides definitive spectroscopic confirmation for the successful application of the dual-

layer TA-Fe and PDTTS coating on the aluminum substrate, corroborating the morphological evidence obtained from electron microscopy.

In addition, XPS was used to measure and characterize the element types and valence states on the surface of Al@TA-Fe@PDTTS particles, as shown in Fig.7. The full XPS spectrum of Al@TA-Fe@PDTTS shows that the surface layer of Al@TA-Fe@PDTTS contains C, O and F elements (Fig.7a), while the Al peak is not clearly detected. This may be because the surface layer of the aluminum particles is covered by the TA-Fe@PDTTS coating layer, which affects the detection of the internal aluminum element. At the same time, the detection of the Fe element is not obvious, which is mainly due to the low content of Fe in Al@TA-Fe@PDTTS. High-resolution XPS spectra provide detailed chemical bonding information. The C 1s spectrum (Fig. 7b) was deconvoluted into five components corresponding to C-H (284.3 eV), C-C (286.0 eV), O-C=O (287.9 eV), -CF_2 (291.0 eV), and -CF_3 (293.3 eV) species[40], reflecting contributions from both the organic TA matrix and the fluorinated PDTTS layer. The O 1s spectrum (Fig. 7c) was fitted with two peaks assigned to C-O-C (531.0 eV) and -OH (532.6 eV) groups, characteristic of the tannic acid component. The F 1s spectrum (Fig. 7d) displays a single peak at 688.7 eV, attributed to covalent C-F bonds from the fluorosilane coating.The above results further show that Al@TA-Fe@PDTTS has a dual core-shell structure.

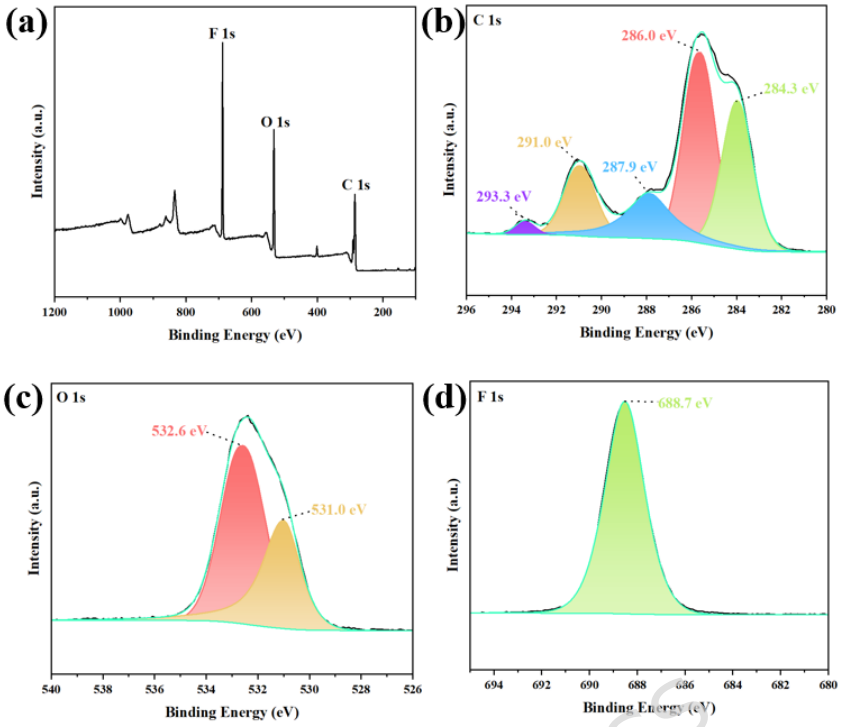

Fig. 7 Survey XPS binding energy spectra and the high-resolution XPS spectra of C 1s, O 1s, and F 1s peaks of Al@TA-Fe@PDTTS.

3.3 Interface performance of Al@TA-Fe@PDTTS

In order to observe the interfacial properties of Al and Al@TA-Fe@PDTTS, the contact between Al and Al@TA-Fe@PDTTS and water was studied in detail, as shown in Fig.8. Pure Al gradually settles to the bottom of the water after being added to the water, and is dispersed in the water to form a suspension after vigorous shaking. In contrast, Al@TA-Fe@PDTTS float directly on the water after being added to water. Even after violent shaking, Al@TA-Fe@PDTTS can still float on the water. This result shows that the surface property of Al@TA-Fe@PDTTS has changed significantly relative to pure Al, In addition, it can also be concluded that the coating of Al@TA-Fe by PDTTS is dense.

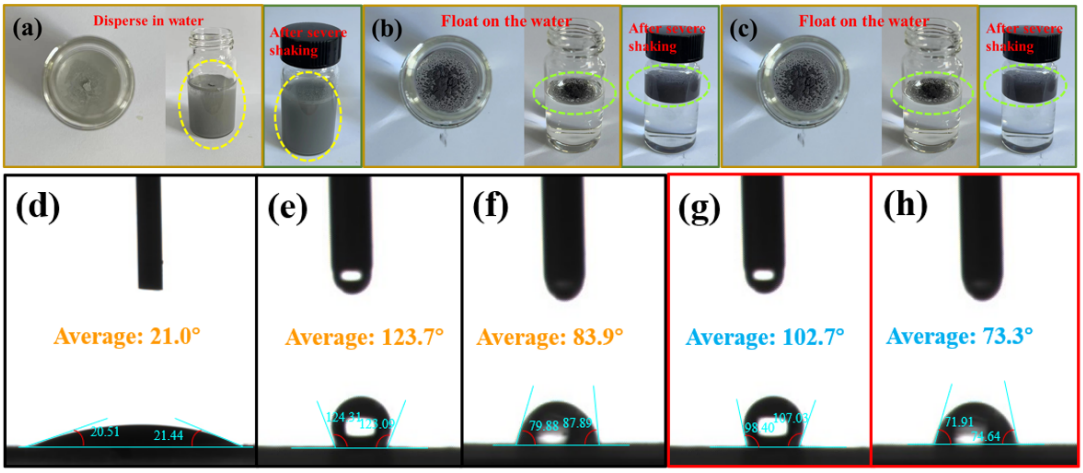

Fig. 8 Photographs of (a) Al, (b) Al@PDTTS and (c) Al@TA-Fe@PDTTS entering the water, and after severe shaking; Static water contact angles of (d) Al, (e) Al@TA-Fe@PDTTS and (f) Al@PDTTS, and (g) Al@TA-Fe@PDTTS and (h) Al@PDTTS after 30 days in water.

In addition, the static contact angles of the samples with water were tested, as shown in Fig.8. Pure Al powder exhibited strong hydrophilicity with an average contact angle of only 21.0°. In contrast, surface modification drastically enhanced hydrophobicity: Al@PDTTS and Al@TA-Fe@PDTTS showed average angles of 83.9° and 123.7°, respectively. This hydrophobicity demonstrated notable persistence, retaining values of 73.3° and 102.7° even after 30 days of water immersion. The consistently higher contact angle of Al@TA-Fe@PDTTS compared to Al@PDTTS indicates that the TA-Fe intermediate layer promotes a more uniform and effective coating of the hydrophobic PDTTS layer on the aluminum surface. These results confirm that the surface is enriched with hydrophobic carbon and fluorine moieties, endowing Al@TA-Fe@PDTTS with superior hydrophobicity and corrosion resistance relative to unmodified aluminum powder[41].

3.4 Thermal reaction properties of Al@TA-Fe@PDTTS

Fig.9 shows the DSC/TG curves of Al and Al@TA-Fe@PDTTS in an argon atmosphere. In the temperature range of 0-800 °C, pure aluminum powder has a melting endothermic peak at 660 °C and no weight loss process. According to the thermogravimetric analysis of the sample in an argon atmosphere (Fig.9), the total mass loss caused by the decomposition of the TA-Fe and

PDTTS coatings is approximately 25 wt%. Therefore, the content of active metal Al in the Al@TA-Fe@PDTTS composite material is approximately 75 wt%. The DSC curve of Al@TA-Fe@PDTTS shows that the peak at 327.7 °C is the decomposition peak of TA, followed by a small exothermic peak for the decomposition peak of PDTTS; the peak at 660 °C is the characteristic endothermic peak of aluminum. The peak at 653 °C is the redox exothermic peak generated by the reaction between aluminum and the decomposition products of TA and PDTTS coating. The thermal decomposition behavior of Al@TA-Fe@PDTTS was elucidated by thermogravimetric (TG) analysis. A gradual weight loss initiates at approximately 110 °C, attributable primarily to the initial thermal decomposition of the tannic acid (TA) component. A pronounced acceleration in mass loss occurs around 300 °C, coinciding with the continued decomposition of TA and the onset of thermal degradation for the PDTTS layer[42]. This major mass loss stage concludes near 510 °C, with the maximum total weight loss of about 25 wt% attained at 550 °C. Notably, a brief mass gain is observed between 610 °C and 655 °C. This mass gain corresponds temporally to a distinct redox exothermic peak at 653 °C in the DSC curve. Collectively, these results demonstrate that the Al@TA-Fe@PDTTS composite undergoes exothermic reactions and associated mass changes well below the melting point of aluminum (660 °C). The heat released from these pre-melting reactions can thereby facilitate and promote the subsequent oxidation of the metallic aluminum core, a process not observed for pristine aluminum powder under the same conditions.

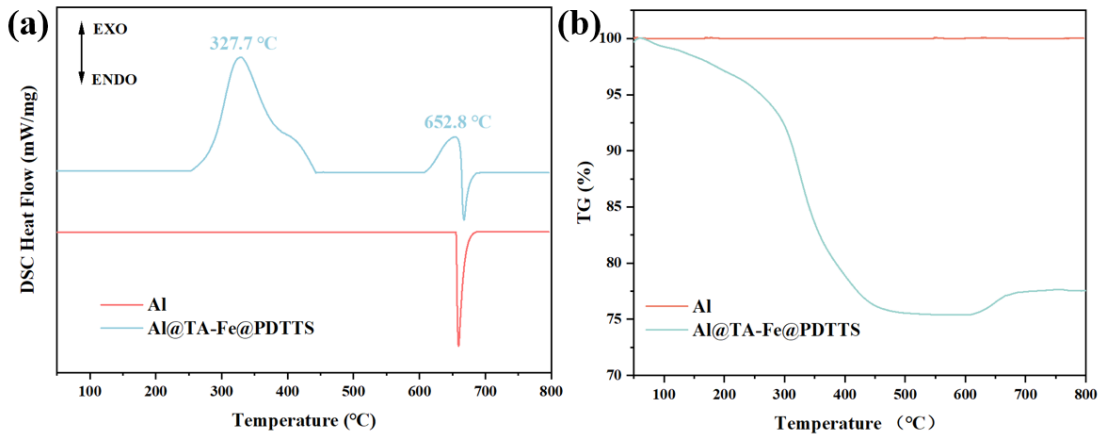

Fig. 9 TG/DSC curves of Al and Al@TA-Fe@PDTTS with the heating rate of 10 K/min in the Ar atmosphere.

In addition, the combustion characteristics of both pure Al and the Al@TA-Fe@PDTTS composite were evaluated in air. Samples were heated at 600 °C and 800 °C for 10 min under ambient atmosphere, after which the solid residues were collected for morphological analysis. As shown in Fig.10, SEM images of the pure aluminum powder after treatment at 600 °C reveal that most particles largely retained their original spherical morphology, indicating limited oxidation. Even at 800 °C, only a minor fraction of the pure Al particles exhibited signs of shell fracture, with the majority remaining intact and spherical. These observations confirm that pure aluminum powder undergoes minimal oxidation in air, even at elevated temperatures.

In striking contrast, the Al@TA-Fe@PDTTS composite displayed markedly different behavior. After exposure at 600 °C, a substantial portion of the particles had transformed into irregular fragments, deviating completely from the initial spherical shape. When the temperature was raised to 800 °C, this fragmentation became predominant, yielding a large quantity of irregular debris. The onset of pronounced morphological change at temperatures below the melting point of aluminum (660 °C) demonstrates that the TA-Fe@PDTTS dual-interface layer effectively destabilizes the native oxide shell and promotes the oxidation of the underlying aluminum core.

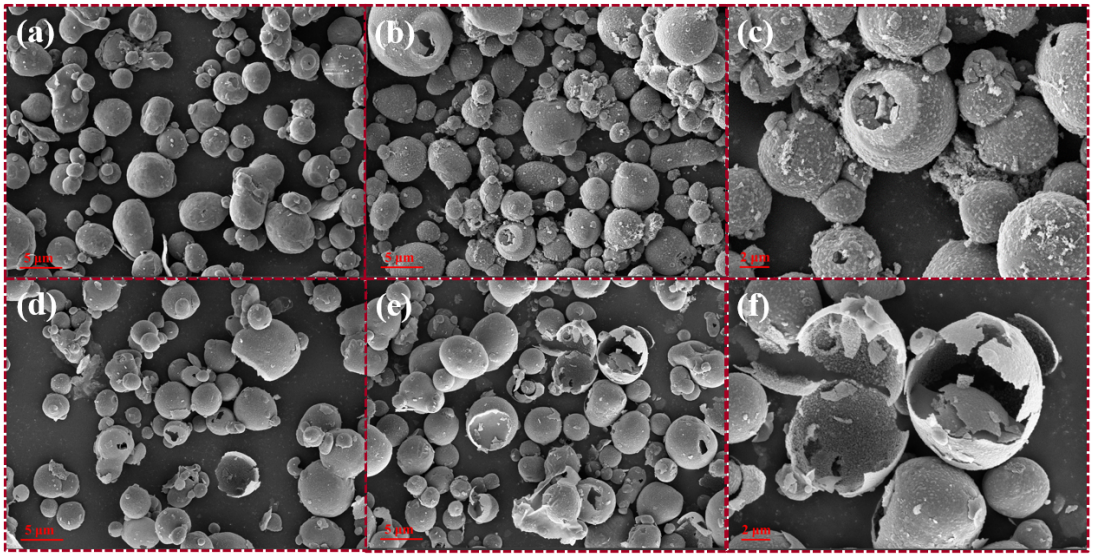

Fig. 10 SEM images of the reaction products: (a) Al powder at 600 °C; (b) Al powder at 800 °C; (c) Magnified view of Al powder at 800 °C; (d) Al@TA-Fe@PDTTS at 600 °C; (e) Al@TA-Fe@PDTTS at 800 °C; (f) Magnified view of Al@TA-Fe@PDTTS at 800 °C. All reactions were conducted in air atmosphere.

X-ray diffraction (XRD) was employed to analyze the phase composition of the combustion residues from Al@TA-Fe@PDTTS (Fig.11). The diffraction patterns indicate that the primary product is crystalline Al_2O_3, accompanied by minor phases of AlF_3 and residual unreacted Al. This phase assemblage confirms that fluorine, released from the thermal decomposition of the PDTTS coating, actively participates in the oxidation process of aluminum. The formation of AlF_3 is particularly significant; its characteristic porous structure substantially increases the interfacial contact area between the remaining aluminum and the ambient oxidant. Furthermore, the porous network facilitates the diffusion of aluminum species, thereby accelerating the energy release rate and enhancing the overall combustion kinetics[22]. Collectively, these findings demonstrate that the TA-Fe@PDTTS dual coating effectively promotes the oxidation of aluminum. Notably, it enables and catalyzes this oxidation reaction at temperatures below the melting point of aluminum[13,18,43].

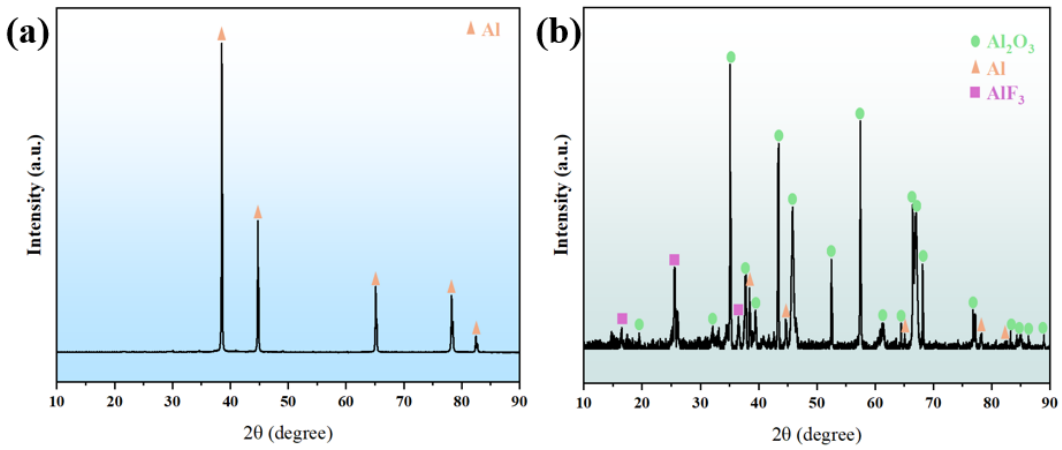

Fig. 11 XRD patterns of the calcined products obtained at 800 °C: (a) Pure Al; (b) Al@TA-Fe@PDTTS.

Based on the comprehensive thermal analysis, combustion product characterization, a stepwise reaction mechanism for Al@TA-Fe@PDTTS during heating is proposed.

Firstly, coating decomposition and reactive species generation (300 – 500 °C): Upon heating, the outer PDTTS layer and the inner TA-Fe network undergo sequential thermal decomposition. The TA-Fe complex decomposes first (~327 °C), followed by PDTTS decomposition (Reactions 2 &3) at slightly higher temperatures. These processes release gaseous products and highly reactive fluorine-containing radicals (e.g., F·, C_XF·) and fluorocarbon fragments crucially.

$$\text{A-e Network} \xrightarrow{\Delta} \text{ases (O, C}_2\text{, }_2\text{)} + \text{Fe-ontaining residues} \quad (2)$$

$$\text{DTTS} \xrightarrow{\Delta} \text{i}_2 + \mathbf{C_X}\text{·()} + \text{F}\cdot\text{(adicals)} + \text{Hydrocarbons} \quad (3)$$

Besides, oxide shell corrosion and cracking (500 – 660 °C): The released fluorine species diffuse through defects in the native Al_2O_3 shell and aggressively react with it. This fluorination reaction converts the high-melting-point Al_2O_3 into volatile AlF_3(Reactions 4). The formation and subsequent sublimation of AlF_3 create and widen pores and cracks within the inert oxide shell, significantly compromising its integrity and barrier function.

$$□□_2□_3(□) + 6□ \cdot (\text{or } □_x□ \cdot) \rightarrow 2□□_3(□) + 3 /2□_2(□) \quad \text{(or other oxygenated products)} \qquad \textbf{(4)}$$

Finally, enhanced aluminum oxidation (Above 660 °C and even below): The cracked and weakened oxide shell can no longer effectively protect the metallic Al core. Oxygen from the environment (or released during earlier decomposition steps) can now readily access the fresh Al surface through the channels created[14-15]. This leads to a strongly exothermic oxidation reaction (Reaction5). Notably, the heat released from the exothermic coating decomposition and the initial fluorination reactions (evident as the exothermic peak at 653 °C in DSC) can pre-heat the particle, enabling the onset of significant Al oxidation even slightly below its bulk melting point (660 °C), as observed in the 600 °C furnace experiments.

$$4□□(□) + 3□_2(□) \rightarrow 2□□_2□_3(□) \qquad \textbf{(5)}$$

This synergistic mechanism-where the coating acts both as a fluorine source to corrode the oxide barrier and as a pre-ignition fuel to provide local heating-effectively overcomes the ignition and combustion limitations of conventional Al powder. The entire process is shown in Fig.12.

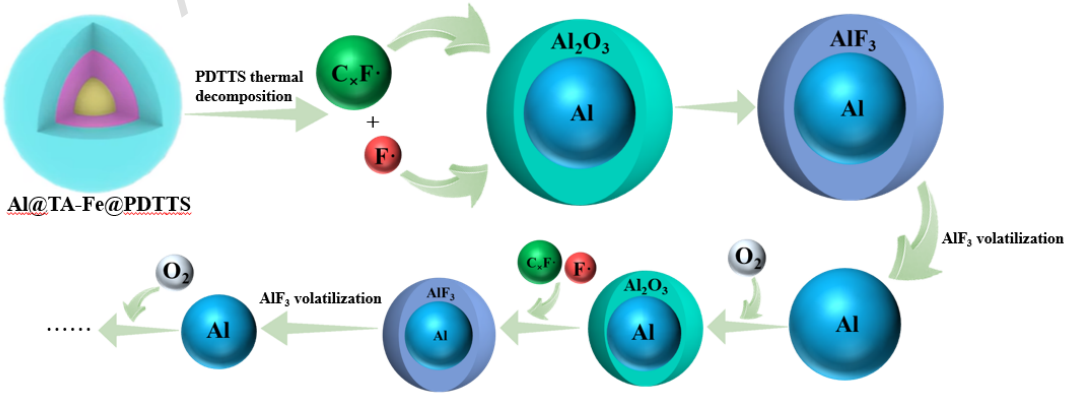

Fig. 12 Schematic diagram of the mechanism of aluminum combustion catalyzed by TA-Fe@PDTTS

3.5 Effect of Al@TA-Fe@PDTTS on catalytic thermal decomposition of AP

In order to study the catalytic decomposition of AP by Al@TA-Fe@PDTTS, Al@TA-Fe@PDTTS and AP were mixed at a mass ratio of 9:1, and then Al@TA-Fe@PDTTS/AP and AP were performed DSC analysis in an Ar atmosphere., as shown in Fig.13. It can be seen from the DSC curve that Al@TA-Fe@PDTTS/AP and AP have one endothermic peak and two exothermic peaks. The endothermic peak at 247 °C is formed by the transformation of AP from an orthorhombic structure to a cubic structure. After adding Al@TA-Fe@PDTTS, the high temperature decomposition peak of AP dropped from 422.3 °C to 380.4 °C. In addition, the exothermic peak of the high-temperature decomposition stage of AP in Al@TA-Fe@PDTTS/AP is much larger than that of pure AP, which may be due to two reasons. One is that the decomposition temperature range of TA-Fe@PDTTS coincides with the high-temperature decomposition range of AP, and the other is that the TA-Fe layer significantly improves the thermal decomposition stage of AP. The results show that Al@TA-Fe@PDTTS can significantly reduce the peak temperature of high-temperature decomposition of AP.

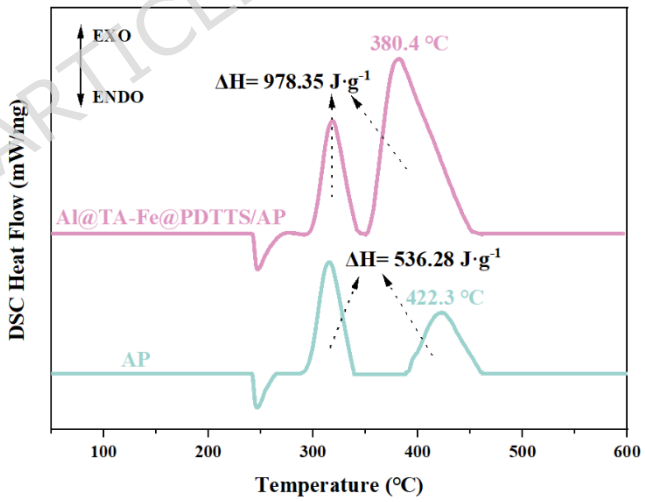

Fig.13 DSC curves of pure AP and Al@TA-Fe@PDTTS/AP with the heating rate of 10 K·min^{-1} in the Ar atmosphere.

The heat release of combustion is an important parameter for measuring the energy materials. The energy release level of energetic materials can be intuitively seen through the combustion heat value. The combustion heat of Al/AP and Al@TA-Fe@PDTTS/AP mixtures was measured under different

oxygen pressures (3 MPa, 2 MPa, 1 MPa, and 0.5 MPa) using an oxygen bomb calorimeter. Each sample was measured three times and the average value was taken. The results are shown in Fig.14. It can be found that when the oxygen pressure dropped from 3 MPa to 1 MPa, the combustion heat values of both samples decreased slightly. Under the same oxygen pressure, the combustion heat value of Al@TA-Fe@PDTTS/AP is always slightly higher than that of Al/AP. This is because although the composite structure can promote heat and mass transfer[44], since the combustion of aluminum powder in an oxygen-rich environment is relatively complete, the introduction of TA-Fe and PDTTS coatings has limited effect on the improvement of the combustion heat value of Al. When the oxygen pressure drops from 1 MPa to 0.5 MPa, the combustion heat value of the Al/AP and Al@TA-Fe@PDTTS/AP mixtures decreases significantly from 25.716 kJ·mol^{-1} and 26.027 kJ·mol^{-1} (the difference between the two is 0.311 kJ·mol^{-1}) to 22.331 kJ·mol^{-1} and 23.728 kJ·mol^{-1} (the difference between the two is 1.397 kJ·mol^{-1}). The above results show that the coating layer on the surface of aluminum powder has a more significant effect on the combustion of aluminum powder in a low-oxygen environment, which also confirms our previous analysis of the thermal decomposition mechanism of Al@TA-Fe@PDTTS during heating.

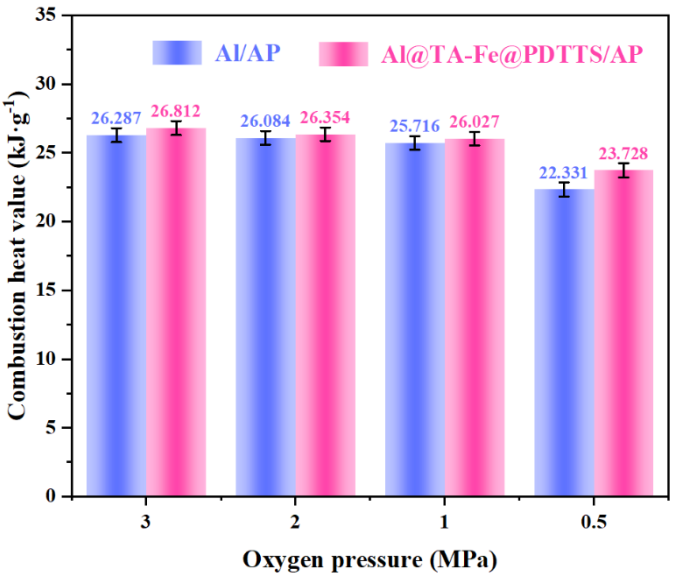

Fig.14 Combustion heat values of samples at different oxygen pressures.

Ignition delay time is one of the indicators of ignition reliability and one of the important factors affecting the tactical performance and accuracy of energetic materials and equipment. The ignition delay time here is defined as the time delay required for the sample to ignite and burn normally after receiving laser energy stimulation. In the laser ignition experiment, the time difference between the appearance of the laser signal and the appearance of the sample ignition signal is identified as the ignition delay time. The results are shown in Fig.S4. The ignition delay times of Al/AP and Al@TA-Fe@PDTTS/AP are 13.2 ms and 4.8 ms, respectively. The introduction of TA-Fe and PDTTS coating layers can effectively shorten the ignition delay time of the mixture.

Besides, the performance metrics of the Al@TA-Fe@PDTTS composite (including exotherm onset, total energy release, ignition delay time, and combustion duration) have been systematically compared with those of typical coated aluminum powder systems reported in the literature. The results are presented in Table 2.

Table 2 The performance metrics of typical coated aluminum powder systems

Composite System	Exotherm Onset (°C)	Total Energy Release(DSC)	Ignition Delay Time	Combustion Duration	Contact Angle	Ref
Al@TA-Fe@PDTTS	653	978.35J/g	4.8 ms	>500 ms	123.7°	This work
Al@TA-Fe@PVDF	494	-	-	-	79.21°	20
Al@PVDF	480.27	480.27 J/g	16 ms	79 ms	-	18
Al@PTFE	386	2.43 kJ/g	-	-	118°	16,17
AI@APFO	597	12.6 kJ/g	0.45 s	-	-	24

The combustion process of Al/AP and Al@TA-Fe@PDTTS/AP is shown in Fig.15. The combustion time of the Al/AP mixture is 250 ms, while the combustion time of the Al@TA-Fe@PDTTS/AP mixture exceeds 500 ms. Comparing the combustion of the two samples, in the combustion process of the Al/AP mixture, the intense combustion lasts for a shorter time and the

flame formed is smaller. The combustion of the Al@TA-Fe@PDTTS/AP mixture is more intense, the combustion area formed is larger, and the intense combustion lasts for a longer time. Compared with Al/AP, Al@TA-Fe@PDTTS/AP starts to burn violently earlier and forms more sparks. The above results show that the composite structure of Al@TA-Fe@PDTTS has a larger contact area, which is conducive to heat and mass transfer, resulting in a faster combustion response of the mixture and a higher degree of combustion.

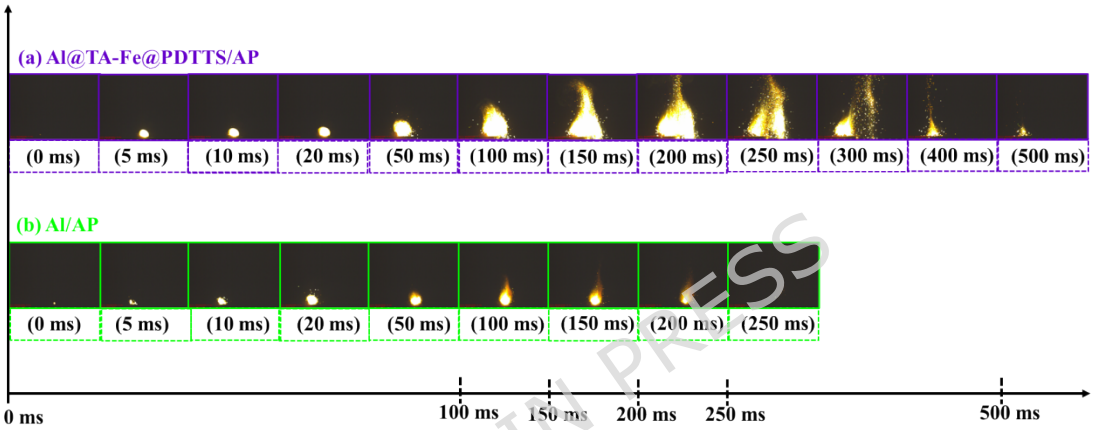

Fig.15 Laser ignition combustion process of Al/AP and Al@TA-Fe@PDTTS/AP samples.

4. Conclusion

In this paper, a dual core-shell structured aluminum-based composite, denoted as Al@TA-Fe@PDTTS, was successfully fabricated. Comprehensive morphological and compositional analyses confirm the uniform deposition of both the inner TA-Fe coordination layer and the outer fluorosilane (PDTTS) shell onto the aluminum particles. This engineered surface imparts significantly enhance hydrophobicity to the composite compared to pure aluminum powder. Molecular dynamics simulations provide theoretical support for the coating stability, revealing a substantial binding energy of 498.21 kcal·mol^{-1} between PDTTS and the TA layer, and an even stronger interaction of 782.36 kcal·mol^{-1} between TA and the native Al_2O_3 surface.

The dual coating profoundly alters the high-temperature reaction pathway

of aluminum. It enables the oxidation of aluminum to initiate below its melting point in an air atmosphere. When combined with AP, the Al@TA-Fe@PDTTS composite acts as a potent catalyst, lowering the peak high-temperature decomposition temperature of AP by 41.9 °C. Furthermore, the Al@TA-Fe@PDTTS/AP mixture exhibits a consistently higher combustion calorific value than the conventional Al/AP blend, with the performance advantage being particularly pronounced under low-oxygen-pressure conditions. Combustion diagnostics verify that the composite mixture has a faster reaction rate and more complete combustion, evidenced by a drastic reduction in ignition delay time from 13.2 ms to 4.8 ms.

Declaration of competing interest

The authors declare that they have no known competing financial interests or personal relationships that could have appeared to influence the work reported in this paper.

Funding

This work was supported by the National Natural Science Foundation of China [grant number 22175026].

Role of the funding source The funding agency had no role in the study design, collection, analysis, interpretation of data, writing of the manuscript, or decision to submit it for publication.

Credit authorship contribution statement

Bo Liu: Methodology, Data curation, Formal analysis, Writing-original draft, Writing-review & editing. **Xiaodong Gou:** Formal analysis, Data curation. **Yingjun Li:** Conceptualization. **Jiahao Liang:** Data curation. **Shi Yan:** Project administration. **Xueyong Guo:** Resources, Project administration. **Jianxin Nie:** Investigation, Resources, Project administration.

Acknowledgements

The authors thank National Natural Science Foundation of China [grant number 22175026] for technical assistance.

Data availability

Data will be made available on request.

References

[1] D. Trache, F. Maggi, I. Palmucci, L.T. DeLuca, Thermal behavior and decomposition kinetics of composite solid propellants in the presence of amide burning rate suppressants, Journal of Thermal Analysis and Calorimetry 132 (2018) 1601-1615.

[2] J. Yuan, J. Liu, Y. Zhou, Y. Zhang, K. Cen, Thermal decomposition and combustion characteristics of Al/AP/HTPB propellant, Journal of Thermal Analysis and Calorimetry 143 (2021) 3935-3944.

[3] D.-L. Xiang, J.-L. Rong, X. He, Detonation performance of four groups of aluminized explosives, Central European Journal of Energetic Materials 13(4) (2016) 903-915.

[4] K.K. Miller, J.L. Gottfried, S.D. Walck, M.L. Pantoya, C.-C. Wu, Plasma surface treatment of aluminum nanoparticles for energetic material applications, Combustion and Flame 206 (2019) 211-213.

[5] C. Huang, Z. Yang, Y. Li, B. Zheng, Q. Yan, L. Guan, G. Luo, S. Li, F. Nie, Incorporation of high explosives into nano-aluminum based microspheres to improve reactivity, Chemical Engineering Journal 383 (2020) 123110.

[6] G. Young, H. Wang, M.R. Zachariah, Application of nano-aluminum/nitrocellulose mesoparticles in composite solid rocket propellants, Propellants, Explosives, Pyrotechnics 40(3) (2015) 413-418.

[7] W. He, B. Tao, Z. Yang, G. Yang, X. Guo, P.-J. Liu, Q.-L. Yan, Mussel-inspired polydopamine-directed crystal growth of core-shell n-Al@PDA@CuO metastable intermixed composites, Chemical Engineering Journal 369 (2019) 1093-1101.

[8] W. He, Z.-H. Li, S. Chen, G. Yang, Z. Yang, P.-J. Liu, Q.-L. Yan, Energetic metastable n-Al@PVDF/EMOF composite nanofibers with improved combustion performances, Chemical Engineering Journal 383 (2020) 123146.

[9] M. Gaurav, P. Ramakrishna, Effect of mechanical activation of high specific surface area aluminium with PTFE on composite solid propellant, Combustion and Flame 166 (2016) 203-215.

[10] M.W. Beckstead, Y. Liang, K. Pudduppakkam, Numerical simulation of single aluminum particle combustion, Combustion, Explosion and Shock Waves 41 (2005) 622-638.

[11] T. Yan, H. Ren, Y. Li, H. Wang, Q. Jiao, Tailoring structural energetics for enhanced reactivity of nano-Aluminum particles based microspheres, Advanced Engineering Materials 21(8) (2019) 1900176.

[12] L. DeLuca, L. Galfetti, G. Colombo, F. Maggi, A. Bandera, V. Babuk, V. Sinditskii, Microstructure effects in aluminized solid rocket propellants, Journal of propulsion and power 26(4) (2010) 724-732.

[13] J.B. DeLisio, X. Hu, T. Wu, G.C. Egan, G. Young, M.R. Zachariah, Probing the reaction mechanism of aluminum/poly (vinylidene fluoride) composites, The Journal of Physical Chemistry B 120(24) (2016) 5534-5542.

[14] P. Liu, X. Li, L. Cheng, X. Zhu, Y. Li, D. Song, Preparation and characterization of n-Al/FeF_3 nanothermite, Chemical Engineering Journal 331 (2018) 850-855.

[15] R. Padhye, A.J. Aquino, D. Tunega, M.L. Pantoya, Fluorination of an alumina surface: modeling aluminum–fluorine reaction mechanisms, ACS applied materials & interfaces 9(28) (2017) 24290-24297.

[16] W. He, P.-J. Liu, F. Gong, B. Tao, J. Gu, Z. Yang, Q.-L. Yan, Tuning the reactivity of metastable intermixed composite n-Al/PTFE by polydopamine interfacial control, ACS applied materials & interfaces 10(38) (2018) 32849-32858.

[17] J. Wang, Z. Qiao, Y. Yang, J. Shen, Z. Long, Z. Li, X. Cui, G. Yang, Core–Shell Al-Polytetrafluoroethylene (PTFE) Configurations to Enhance Reaction

Kinetics and Energy Performance for Nanoenergetic Materials, Chemistry–A European Journal 22(1) (2016) 279-284.

[18] Y. Li, J. Li, B. Wang, H. Ma, Z. Han, An approach to the induced reaction mechanism of the combustion of the nano-Al/PVDF composite particles, Surface and Coatings Technology 429 (2022) 127912.

[19] H. Wang, J. Shen, D.J. Kline, N. Eckman, N.R. Agrawal, T. Wu, P. Wang, M.R. Zachariah, Direct writing of a 90 wt% particle loading nanothermite, Advanced Materials 31(23) (2019) 1806575.

[20] X. Ke, S. Guo, G. Zhang, X. Zhou, L. Xiao, G. Hao, N. Wang, W. Jiang, Safe preparation, energetic performance and reaction mechanism of corrosion-resistant Al/PVDF nanocomposite films, Journal of Materials Chemistry A 6(36) (2018) 17713-17723.

[21] H. Wang, D.J. Kline, M. Rehwoldt, T. Wu, W. Zhao, X. Wang, M.R. Zachariah, Architecture can significantly alter the energy release rate from nanocomposite energetics, ACS Applied Polymer Materials 1(5) (2019) 982-989.

[22] J. Wang, Y. Qu, F. Gong, J. Shen, L. Zhang, A promising strategy to obtain high energy output and combustion properties by self-activation of nano-Al, Combustion and Flame 204 (2019) 220-226.

[23] X. Ke, S. Guo, B. Gou, N. Wang, X. Zhou, L. Xiao, G. Hao, W. Jiang, Superhydrophobic fluorine-containing protective coating to endow Al nanoparticles with long-term storage stability and self-activation reaction capability, Advanced Materials Interfaces 6(19) (2019) 1901025.

[24] Y. Ou, Q. Jiao, N. Li, S. Yan, R. Yang, Pyrolysis of ammonium perfluorooctanoate (APFO) and its interaction with nano-aluminum, Chemical Engineering Journal 403 (2021) 126367.

[25] T.R. Sippel, S.F. Son, L.J. Groven, Aluminum agglomeration reduction in a composite propellant using tailored Al/PTFE particles, Combustion and Flame 161(1) (2014) 311-321.

[26] S.K. Valluri, M. Schoenitz, E.L. Dreizin, Metal-rich aluminum-

polytetrafluoroethylene reactive composite powders prepared by mechanical milling at different temperatures, Journal of Materials Science 52 (2017) 7452-7465.

[27] P. M. Gandhi, S. Das, M. Schoenitz, E. L. Dreizin, Aluminum powders with modified morphology and enhanced reactivity prepared by emulsion-assisted milling, Combustion and Flame 275 (2025) 114116.

[28] N. Li, Z. Geng, M. Cao, L. Ren, X. Zhao, B. Liu, Y. Tian, C. Hu, Well-dispersed ultrafine Mn3O4 nanoparticles on graphene as a promising catalyst for the thermal decomposition of ammonium perchlorate, Carbon 54 (2013) 124-132.

[29] R.R. Salunkhe, J. Tang, Y. Kamachi, T. Nakato, J.H. Kim, Y. Yamauchi, Asymmetric supercapacitors using 3D nanoporous carbon and cobalt oxide electrodes synthesized from a single metal–organic framework, ACS nano 9(6) (2015) 6288-6296.

[30] G. Duan, X. Yang, J. Chen, G. Huang, L. Lu, X. Wang, The catalytic effect of nanosized MgO on the decomposition of ammonium perchlorate, Powder technology 172(1) (2007) 27-29.

[31] Y. Hu, B. Tao, F. Shang, M. Zhou, D. Hao, R. Fan, D. Xia, Y. Yang, A. Pang, K. Lin, Thermal decomposition of ammonium perchlorate over perovskite catalysts: Catalytic decomposition behavior, mechanism and application, Applied Surface Science 513 (2020) 145849.

[32] X. Gou, W. Liu, Y. Xu, Z. Ma, X. Zhang, J. Zhang, Electrochemical Synthesis of the Energetic Combustion Catalyst Co (BODN)·9H_2O and Its Catalytic Effect on Ammonium Perchlorate Thermal Decomposition, Langmuir 39(48) (2023) 17498-17512.

[33] X. Gou, Z. Ma, W. Liu, X. Zhang, C. Chen, J. Zhang, F. Xiao, X. Zhang, Preparation of AP@ ZIF-7 composite materials by chemical precipitation method: A good strategy for simultaneously improving its thermal performance, energy property and moisture absorption, Powder Technology 433 (2024) 119230.

[34] X. Gou, W. Liu, J. Zheng, W. Tang, B. Xu, Z. Ma, C. Chen, F. Xiao, J. Zhang, Enhanced thermal, safety and anti-hygroscopicity performance of core-shell ammonium perchlorate with a double coating layer, Dalton Transactions 52(46) (2023) 17324-17339.

[35] G. Xiaodong, L. Wei, M. Zhongliang, Z. Mengqi, L. Xiaoyu, Z. Xuan, In-situ synthesis of AP@Co/BIM composites with improved thermal performance and anti-hygroscopicity, Materials Chemistry and Physics 309 (2023) 128347.

[36] T. Zeng, D. Li, Y. Lan, W. Gao, J. Li, R. Yang, Study on interaction between propargyl-terminated polybutadiene and plasticizers based on simulation and experiments, The Journal of Physical Chemistry A 123(29) (2019) 6370-6377.

[37] J.-s. Mao, B.-g. Wang, Y.-f. Chen, J.-b. Fu, X. Tian, B.-y. Ye, Molecular dynamics simulation of CL-20/DNDAP cocrystal-based PBXs, Journal of Molecular Modeling 29(7) (2023) 199.

[38] Q. Zhu, T. Wang, X. Sun, Y. Wei, S. Zhang, X. Wang, L. Luo, Effects of fluorine-based modification on triboelectric properties of cellulose, Polymers 14(17) (2022) 3536.

[39] J. Guo, Y. Ping, H. Ejima, K. Alt, M. Meissner, J.J. Richardson, Y. Yan, K. Peter, D. Von Elverfeldt, C.E. Hagemeyer, Engineering multifunctional capsules through the assembly of metal–phenolic networks, Angewandte Chemie International Edition 53(22) (2014) 5546-5551.

[40] S. Nie, Q. Fu, X. Lin, C. Zhang, Y. Lu, S. Wang, Enhanced performance of a cellulose nanofibrils-based triboelectric nanogenerator by tuning the surface polarizability and hydrophobicity, Chemical Engineering Journal 404 (2021) 126512.

[41] F. Xiao, H. Zhang, W. Liu, J. Zhang, T. Liang, J. Hu, Y. Zhang, P. Luo, Enhanced combustion performance of core-shell aluminum with poly (vinylidene fluoride) interfacial layer: Constructing the combination bridge of aluminum powder and poly (vinylidene fluoride), Surface and Coatings Technology 439 (2022) 128410.

[42] S. Chen, H. Yu, W. Zhang, R. Shen, W. Guo, L.T. DeLuca, H. Wang, Y. Ye,

Sponge-like Al/PVDF films with laser sensitivity and high combustion performance prepared by rapid phase inversion, Chemical Engineering Journal 396 (2020) 124962.

[43] N. Kostoglou, I.E. Gunduz, T. Isik, V. Ortalan, G. Constantinides, A.G. Kontos, T. Steriotis, V. Ryzhkov, E. Bousser, A. Matthews, Novel combustion synthesis of carbon foam-aluminum fluoride nanocomposite materials, Materials & Design 144 (2018) 222-228.

[44] L. Xie, J. Liu, Q. Jiao, X. Nie, H. Ren, Enhance thermal response behavior of energetic composite by doping fluorinated graphene, Combustion and Flame 265 (2024) 113484.